Kinematics of footwall exhumation at oceanic detachment faults: solid-block rotation and apparent unbending

Dan sandiford[1], Sascha Brune[2], Anne Glerum[2], John Naliboff[3], and Joanne M Whittaker[4]

[1]University of Melbourne
[2]Helmholtz Centre Potsdam GFZ German Research Centre for Geosciences
[3]Unknown
[4]University of Tasmania

November 23, 2022

Abstract

Seafloor spreading at slow rates can be accommodated on large-offset oceanic detachment faults (ODFs), that exhume lower crustal and mantle rocks in footwall domes termed oceanic core complexes (OCCs). Footwall rock experiences large rotation during exhumation, yet important aspects of the kinematics - particularly the relative roles of rigid block rotation and flexure - are not clearly understood. Using a high-resolution numerical model, we explore the exhumation kinematics in the footwall beneath an emergent ODF/OCC. A key feature of the models is that footwall motion is dominated by solid rotation, accommodated by the concave-down ODF. This is attributed to a system behaviour in which the accumulation of distributed plastic strain is minimized. A consequence of these kinematics is that curvature measured along the ODF is representative of a neutral stress configuration, rather than a 'bent' one. Instead, it is in the subsequent process of 'apparent unbending' that significant flexural stresses are developed in the model footwall. The brittle strain associated with apparent unbending is produced dominantly in extension, beneath the OCC, consistent with earthquake clustering observed in the Trans-Atlantic Geotraverse at the Mid-Atlantic Ridge.

Kinematics of footwall exhumation at oceanic detachment faults: solid-block rotation and apparent unbending

Dan Sandiford[1,2], Sascha Brune[2,3], Anne Glerum[2], John Naliboff[4], Joanne M. Whittaker[1]

[1]Institute for Marine and Antarctic Studies, University of Tasmania, Hobart, Tasmania, Australia, 7004
[2]Helmholtz Centre Potsdam - German Research Centre for Geosciences (GFZ)
[3]Institute of Geosciences, University of Potsdam, Potsdam, Germany
[4]Department of Earth and Environmental Science, New Mexico Institute of Mining and Technology

Key Points:

- Numerical models of footwall exhumation show a significant component of solid-block rotation
- Brittle footwall deformation away from the detachment fault is dominated by 'apparent unbending'
- 'Unbending' since curvature gets reduced, 'apparent' as the footwall is not bent in the first place

Corresponding author: Dan Sandiford, dan.sandiford@utas.edu.au

Abstract

Seafloor spreading at slow rates can be accommodated on large-offset oceanic detachment faults (ODFs), that exhume lower crustal and mantle rocks in footwall domes termed oceanic core complexes (OCCs). Footwall rock experiences large rotation during exhumation, yet important aspects of the kinematics - particularly the relative roles of solid-block rotation and flexure - are not clearly understood. Using a high-resolution numerical model, we explore the exhumation kinematics in the footwall beneath an emergent ODF/OCC. A key feature of the models is that footwall motion is dominated by solid-block rotation, accommodated by the concave-down ODF. This is attributed to a system behaviour in which the accumulation of distributed plastic strain is minimized. A consequence of these kinematics is that curvature measured along the ODF is representative of a neutral stress configuration, rather than a 'bent' one. Instead, it is in the subsequent process of 'apparent unbending' that significant flexural stresses are developed in the model footwall. The brittle strain associated with apparent unbending is produced dominantly in extension, beneath the OCC, consistent with earthquake clustering observed in the Trans-Atlantic Geotraverse at the Mid-Atlantic Ridge.

1 Introduction

Slip accumulation on major normal faults, such as those bounding slow spreading ridges, induces rebound and flexure due to unloading within the axial rift (Spencer, 1984; Wernicke & Axen, 1988; Buck, 1988). The flexural deformation may itself produce brittle failure, representing a cascade of deformation from major to subsidiary fault systems. Slow seafloor spreading is often taken up by extension on large-offset asymmetric detachment faults (ODFs), which exhume lower crustal and mantle rocks in domal footwall exposures termed oceanic core complexes (OCCs) (e.g. Cannat (1993); Tucholke (1998)). This study is primarily concerned with the kinematic characteristics of exhumation, the resulting flexural stress and deformation patterns, and the expression of these dynamics in footwall seismicity.

Paleomagnetic inclination data show that footwall blocks in ODF systems undergo significant rotation, typically 50-80°, during exhumation; a process that is often termed rollover (Morris et al., 2009; MacLeod et al., 2011; Garcés & Gee, 2007). What remains unclear, however, is whether the kinematics of exhumation (which ultimately produce these estimated rotations) tend to be dominated by footwall flexure (simple bending), solid-block rotation, or perhaps more complicated internal deformation patterns like flexural slip or vertical simple shear (e.g. Wernicke and Axen (1988)). While the kinematics of exhumation has not received a great deal of attention in ODF settings (cf. continental core-complexes e.g. Wernicke and Axen (1988); Axen and Hartley (1997)) a frequent assumption is that flexure plays an important role in footwall exhumation (e.g. (Tucholke, 1998; MacLeod et al., 2002; Parnell-Turner et al., 2017; Cannat et al., 2019)).

This assumption is true not only in regard to the developmental stage of detachments, where regional flexural-isostatic rebound plays a role in rotating planar normal faults to shallower dips (e.g. Buck (1988)), but also in mature settings, with significant (10s km) fault offset. In this view rollover 'flexes the brittle footwall, such that the upper part of the footwall block is under tension' (Tucholke (1998)). Likewise, the detachment fault itself is thought to 'rotate by flexure to low angles' (MacLeod et al., 2002). Again, ridge-parallel faults that intersect OCCs are often depicted as normal faults related to the inferred flexural tension in the upper part of the footwall (Tucholke et al., 1998; MacLeod et al., 2002, 2009; Escartín et al., 2017; Collins et al., 2012). The inferred relationship between OCC/ODF curvature and footwall flexural stress is what we refer to as an elastic plate model. Such a relationship is completely absent in the numerical models we discuss.

Seismicity provides insight into stress and, particularly, deformation patterns in the brittle lithosphere, and thereby a potential means of constraining kinematics of footwall exhumation. Previous seismicity studies suggest that significant brittle deformation occurs in detachment footwalls as part of exhumation (Demartin et al., 2007; Parnell-Turner et al., 2017). Most records of seismicity in detachment footwalls are dominated by normal-faulting mechanisms and are often attributed to the same far-field tectonic stresses responsible for sustaining the extensional plate boundary (Demartin et al., 2007; Collins et al., 2012; Grevemeyer et al., 2013). Compressional seismicity has also been observed in ODF footwalls, and it is this observation that has been argued to be diagnostic of flexure within the elastic plate framework (Parnell-Turner et al., 2017). However, the identified compressional earthquakes also exhibit significant variability in the orientation of the focal mechanism P-axes. This casts some doubt over whether such events are representative of a 'tectonic' stress state arising from flexure in the detachment system.

In the study of Demartin et al. (2007), which investigated the Trans-Atlantic Geotraverse (TAG) detachment (located on the Mid-Atlantic Ridge at $\sim 26°$ N), focal mechanisms constructed from footwall seismicity are closely aligned with the spreading direction. The authors identified two distinct zones of seismic activity, one interpreted to represent the curved trace of the active detachment fault, and a second locus about 8 km outboard of the detachment cluster, inferred to represent slip on antithetic faults. However, a dynamic explanation for the occurrence of this prominent, spatially-offset zone of deformation within the footwall remains elusive.

In this paper, we investigate the kinematics of footwall exhumation beneath an emergent ODF/OCC system, focusing on results from high-resolution numerical models. In these models, solid-block rotation plays a dominant role in the kinematics of footwall exhumation. Our analysis explores the implications for flexural stress and deformation patterns in the system. In doing so, we provide a potential explanation for the seismicity patterns in the TAG detachment, while questioning the tectonic origin for compressional seismicity at the $13°20'$ N detachment (cf. Parnell-Turner et al. (2017)). Our model suggests that flexural strain is an important component of the seismic moment produced in detachment footwalls, however the spatial relationship between flexural strain and detachment curvature is very different to that assumed in elastic plate models.

2 Numerical experiments

We model the evolution of an amagmatic ODF setting using the open-source finite element code ASPECT version 2.2.0 (see Kronbichler et al. (2012); Heister et al. (2017); Bangerth et al. (2020, 2020b)). To do so, we solve the incompressible Stokes and advection-diffusion equations, in a 2-D domain, subject to boundary conditions on the temperature and velocity. The model is initialised with a thin lithosphere, defined by a transient cooling profile with a thermal age of 0.5 Myr in the center of the domain. The domain is 400 km wide and 100 km deep. The thermal profile ages outwardly in proportion to the applied spreading rate of 2 cm/yr (full rate), which is representative for slow ocean ridges in general and similar to the current spreading rate at the TAG detachment ($\sim$ 2.5 cm/yr) (Müller et al., 2016). Uniform inflow at the bottom boundary balances the outward flux of material at the side boundaries. The model has a free surface (Rose et al., 2017), and a diffusion process is applied to the surface topography in order to counteract strong mesh deformation. The model has a static, hierarchical mesh refinement such that the quadrilateral elements in the cold, brittle part of the model have an edge length of 125 meters, while at the base of the domain the element length is 2 km.

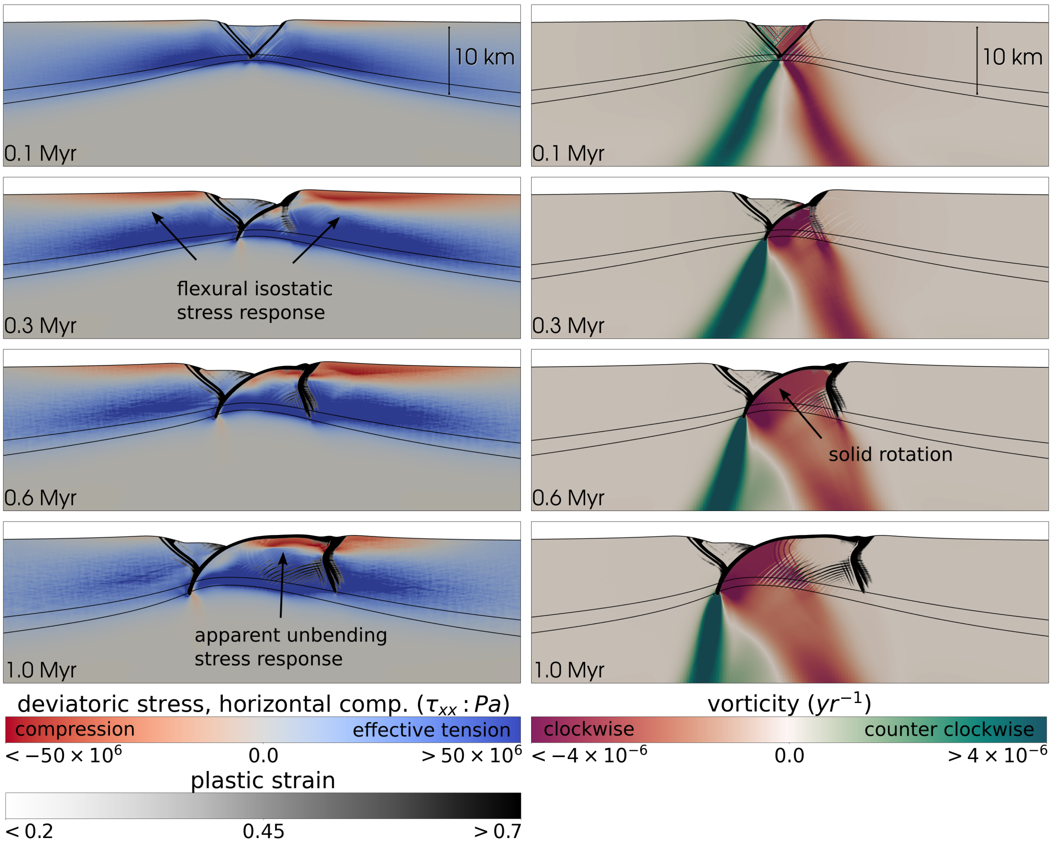

Figure 1. Evolution of reference numerical model from symmetric graben to asymmetric detachment system highlighting the role of solid-block rotation in exhumation as well as flexural processes. The left hand panels show horizontal component (τ_{xx}) of the deviatoric stress tensor, revealing flexural stress accumulation during the development of the ODF and footwall exhumation. The stress tensor definition, for the Maxwell visco-elastic plastic rheology, is discussed in the Supplementary Information. The right hand panels show the vorticity (counter-clockwise rotations are positive), and demonstrate the role of solid-block rotation in exhumation at various stages of the model evolution. The two black lines are contours of the temperature field at 600 and 700 °C. The accumulated plastic strain is shown with a transparent greyscale, showing the location of brittle structures. The full model evolution is animated in Supplementary movie S1.

There is no compositional differentiation in the model (i.e. no crust/mantle). All parts of the domain are subject to the same constitutive model. The constitutive model incorporates viscous (dislocation creep), elastic and plastic (pseudo-brittle) deformation mechanisms, hereafter referred to as visco-elastic plastic (VEP) rheology, following the approach of Moresi et al. (2003). The development and benchmarking of the rheological model was guided by the study of Olive et al. (2016). The dominant deformation mechanism is selected for each element based on the system state (temperature, stress, accumulated strain). A random component of plastic strain is used to localise deformation. Further details and employed parameters are provided in the Supplementary information (Text S2, and Table S1). The ASPECT parameter file used to run the reference model can be downloaded from `https://github.com/dansand/odf_paper`, or from the Supporting Information.

The development of detachment fault systems is associated with the existence of faults that are significantly weaker than the host rock (Reston & Ranero, 2011), while the additional development of rider blocks can depend on the relative amount of weakening in the cohesion versus friction coefficient terms in the yield stress envelope (Choi et al., 2013). Here, we applied weakening of the cohesion and friction angle as well as of the prefactor in the dislocation creep law, similar to recent studies using ASPECT (Glerum et al., 2018; Naliboff et al., 2020).

The reference model (e.g. Fig. 1) develops a large offset OCC (several 10s km), in the absence of rider blocks (see Fig. 4 annotations for clarification) and remains stable (quasi-steady state) for around 1 Myr, until the footwall breaks up and a new detachment emerges. These timescale are consistent with the observed duration of individual OCCs segments (Tucholke et al., 1998). In addition we present an alternative model (e.g. Fig. 4) where the rate of plastic weakening is faster (cohesion/friction angle reduce linearly by factors of 0.5/0.1 over a strain interval of 2, rather than 6). In this model, the footwall shows a greater tendency to break up, similar to previous modelling results (Lavier et al., 2000).

3 Model evolution, kinematics and deformation

3.1 Reference model evolution

Figure 1 shows the evolution of the reference model from a brief stage of symmetrical necking through to a completely asymmetric ODF system. At 0.1 Myr, near-symmetric planar faults are active, producing a graben with minor intra-rift faults. The load (deficit) of the graben is supported through regional flexural-isostatic rebound, as revealed in the horizontal component of the deviatoric stress tensor in the left hand panels of Fig. 1. This is one of two modes of lithospheric flexure exhibited by the model, as discussed later.

At 0.3 Myr the flexural-isostatic response has deformed the active faults, with the deeper parts of each conjugate fault becoming concave-down. At around this point, the model rapidly transitions to asymmetric extension. The right hand fault begins to sole into a wider zone of ductile shear at depth (the brittle-ductile transition occurs between the 600 and 700 °C temperature contours, shown with thin black lines in all Figures). Meanwhile the conjugate fault is abandoned. At this point, the flow of mantle material into the footwall of the active fault develops a strong solid-block rotation component (as shown in the vorticity field, right hand panels Fig. 1).

Beyond 0.3 Myr, slip along the detachment fault leads to the progressive up-dip migration of the breakaway zone, and exposure of the OCC (refer to annotations in Fig. 2 as a guide to terminology). Between $\sim$ 1.0 - 2.0 Myr, the geometry and kinematics of ODF/OCC system reaches quasi-steady state. After about 2.4 Myr, the footwall begins to break up, with an antithetic footwall fault becoming the locus for a new, oppositely-dipping, detachment. This stage of the model development is shown in the Supplementary movie S1.

The early evolution of the ODF in our model shares some important similarities with the flexural rotation model (Buck, 1988). The load produced by the extension (the graben) is accommodated regionally through lithospheric flexure, which in turn deforms the normal fault, initiating a transition from planar fault to concave-down detachment. What is also evident in the numerical model is: a) the way in which detachment fault concavity is closely tied to the development of a rotational flow in the footwall (e.g. Fig. 1 right hand panels); and b) the fact that this rotational flow initiates at depths just beneath the brittle-ductile transition. The development of strong solid-block rotation occurs relatively early in the model evolution ($\sim$ 0.3 Myr). We describe this rotational component of exhumation in more detail in the following section.

3.2 Exhumation kinematics

Figure 2 shows features of the reference model after 1.5 Myr of evolution, with the ODF system in quasi-steady state (in the hanging wall reference frame). In the top panel of Fig. 2, we depict the square root of second invariant (hereafter magnitude) of the strain rate tensor as well as the model velocity vectors. In the bottom panel of Fig. 2, we show the flow vorticity as well as vectors of the translated velocity field (velocity in the hanging wall reference frame).

In the footwall directly beneath the ODF, the combination of relatively high vorticity and low strain rate magnitude indicates flow dominated by solid-block rotation. This rotation is accommodated by the morphology of the active ODF, which approximates a circular arc through much of its active extent. Note that the zone of high vorticity in the footwall extends slightly deeper than the base of the ODF. As we explain in the Discussion, this provides the explanation for why the footwall does not exhibit the stress state anticipated in the elastic stress model (i.e. tension in the upper-most part of the footwall, with compression at greater depths).

With solid-block rotation dominant in the footwall beneath the ODF, and rigid plate motion occurring in the outboard region (i.e, towards the right hand side of the model), it follows that there must be a transitional zone between these flow regimes. In the reference model, this transition occurs as a zone of flexural deformation outboard from the active ODF, beneath the OCC. The flexural nature of the deformation is revealed by the polarised pattern in the horizontal deformation rate (Fig. 3, top panel) with shortening in the upper few kilometers and a significantly larger, triangular zone of active extension in the deeper part of the footwall.

We refer to this zone of flexural deformation as the zone of 'apparent unbending'. 'Unbending' because the flexural strain (change in curvature) is essentially measurable by the straightening of the ODF, 'apparent' because the ODF footwall in our model is not really bent in the first place. In other words, apparent unbending is a stress-accumulating rather than a stress-releasing process, in contrast to the elastic plate model. The spatial relationships between the zone of apparent unbending and ODF curvature is covered in more detail in the Discussion Section.

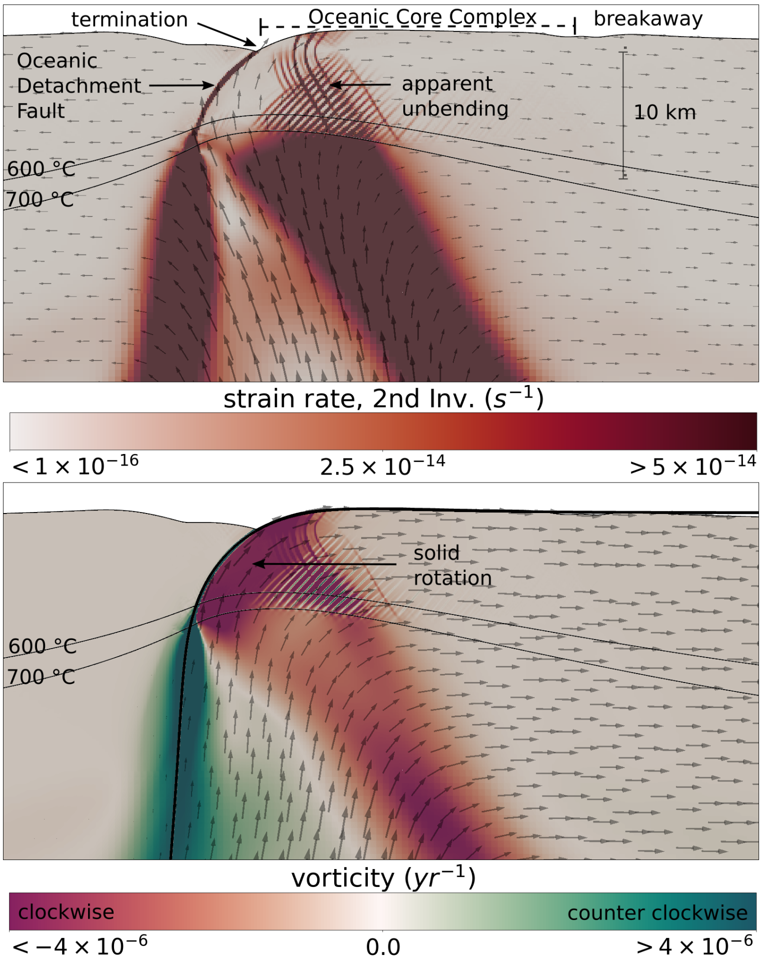

Figure 2. Reference model in quasi-steady state configuration, showing deformation localisation in the footwall outboard from the termination (apparent unbending), and solid-block rotation in the footwall beneath the ODF. Annotations show key features of the detachment system referred to in main text. The top panel shows the magnitude of the strain rate tensor: $|D| = (D_{ij}D_{ij})^{1/2}$; model velocity shown with arrows. Black lines are temperature contours shown at 600 and 700 °C, within which the brittle-ductile transition occurs. The bottom panel shows the flow vorticity; arrows show the velocity in the hanging wall reference frame (in which the system is quasi-steady state). The bold black line following the ODF/OCC is a parameterisation of the detachment geometry, undertaken in post-processing.

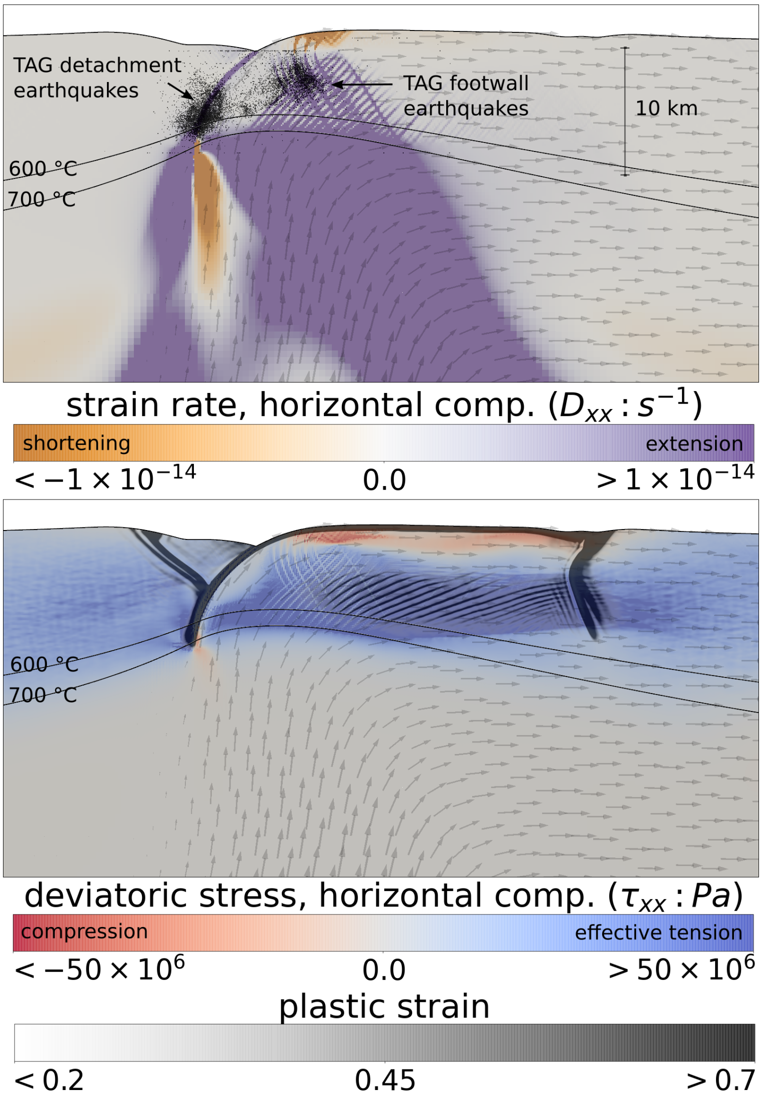

Figure 3. Reference model in quasi-steady state configuration at an elapsed time of 1.5 Myr, showing the strongly localised deformation rates associated with apparent unbending, as well as the stresses developed. Seismicity from the TAG segment is overlain as black dots (from Demartin et al. (2007)). The top panel shows the horizontal component (D_{xx}) of the strain rate tensor. The bottom panel shows the same component of the deviatoric stress tensor. Black lines show temperature contours at 600 and 700 °C. Grey vectors in both panels show the velocity field in the hanging-wall frame of motion.

Figure 3 shows that while stress and strain rates generally share the same sign (are mainly co-axial), deformation tends to be more localised, while the resulting stresses are to an extent 'locked in' to the plate. This is an important observation for thinking about how to interpret patterns of seismicity from a geodynamic perspective; i.e. should variations in seismic moment (or activity rate) be compared with patterns of differential stress or rather strain rates (or a combination of both, e.g. the brittle dissipation)? Our interpretative framework is motivated by Chapple and Forsyth (1979) who argue that seismicity should be viewed as the expression of strain in the brittle regime. In this view, zones of high brittle strain rate, along with the orientation of deformation, are the most relevant quantities to compare to earthquake observations.

3.3 Effects of Rapid Strain Weakening

Figure 4 shows strain rates and vorticity from an alternative model where the rate of plastic weakening is faster (cohesion/friction angle reduce by factors of 0.5/0.1 over a strain interval of 2, rather than 6). This precludes the development of large displacement, quasi-steady state detachment systems. Rather we see more rapid reorganisations, along with various modes of 'rider block' formation and footwall breakup. The model evolution is shown in more detail in Supplementary Movie S2.

Although the alternative model displays greater structural complexity and temporal variability than the reference model the large-scale kinematics are still the same. Exhumation of the footwall is likewise associated with a strong component of solid-block rotation, shown by high (negative) values in the right hand panels of Fig. 4.

In the previous section, we discussed the kinematic requirement that deformation must take place between the exhumation region, where the footwall is dominated by solid-block rotation, and the outboard region where the plate undergoes rigid translation. In the reference model, this transition occurs through a process of brittle flexure, which we term apparent unbending. The alternative model also undergoes periods when the transition occurs through apparent unbending (e.g. snapshots at 0.6, 2.2, and 2.7 Myr). However, the alternative model demonstrates that the kinematic transition can instead occur through slip on a single through-going normal fault. This pattern is shown in the snapshot at 1.3 Myr.

At this point, the footwall does not 'apparently unbend' in a coherent (flexural) manner, but rather it undergoes rotation as an almost-rigid block, bounded by major faults at either end (one being the ODF). The fault at the outboard edge on the right hand side of the block has a concave-up geometry, as is required to accommodate the rotation, in a sense mirroring that of the ODF, and it becomes sub-vertical near its surface exposure. This mode of footwall transition has some similarities with the 'subvertical simple shear' model, arising from an analogous kinematic problem in the context of continental core complexes (Wernicke & Axen, 1988).

Two aspects of the system are notable at this stage (1.3 Myr in Fig. 4). First, the kinematic transition between rotation and translation is achieved without any shallow footwall shortening (unlike in the case of apparent unbending). Secondly, the footwall exposure (OCC) at this stage has a domal shape, where material is rotationally-overturned, such that the slope and velocity vector at the outboard edge of the OCC have a downwards component (velocity vectors are shown in Supplementary movie S2).

4 Discussion

There are two main focus points of our discussion. First we consider flexural processes in our numerical models in more detail, highlighting contrasts with existing models for the flexural stress in ODF systems. Second we compare the modelled patterns of brittle deformation with observations of seismicity.

4.1 Flexural processes in footwall exhumation

Strain rates and stresses in our numerical models suggest an important role for flexure in footwall exhumation. The main locus of flexure in the reference model (e.g. Fig. 3) occurs outboard from the ODF termination, associated with shortening in the upper few kilometers of the OCC/footwall and extension beneath the neutral plane. We describe this process as apparent unbending. This flexural pattern is very different from that expected based on an elastic plate model, which has commonly been invoked for the flexural stress state of the footwall. In this view, rollover *"flexes the brittle footwall, such that the upper part of the footwall block is under tension"* (Tucholke, 1998). Recently, the discovery of compressional earthquake focal mechanisms in an ODF footwall has been interpreted in terms of an elastic plate model (Parnell-Turner et al., 2017). To under-

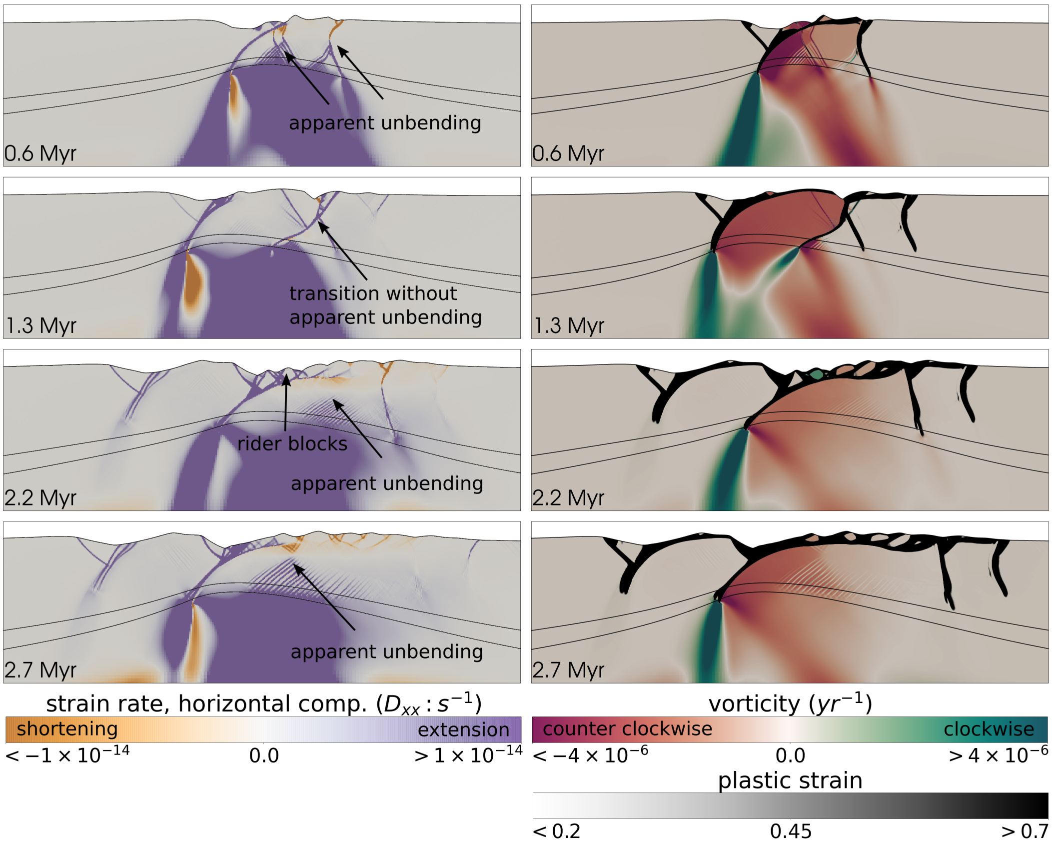

Figure 4. Evolution of model with more rapid strain weakening, showing the predominate role of solid-block rotation in the footwall beneath the ODF, though with greater structural complexity that the reference model. The left hand panels show the horizontal component (D_{xx}) of the strain rate tensor. The right hand panels show the vorticity, along with the accumulated plastic strain in greyscale. The two black lines are contours of the temperature field at 600 and 700 °C. The model evolution is shown in more detail in Supplementary Movie S2

stand the flexure patterns produced in our numerical models, and why these diverge from the expectation of an elastic plate model, we need to carefully consider both the mechanical and kinematic trajectory of the upwelling rock mass during exhumation.

In Figure 1 and 3, we note that the magnitude of the deviatoric stress components increases dramatically at around 700 °C. The temperature range 600-700 °C marks the brittle-ductile transition (BDT) in the numerical model, which globally tends to define the limit of earthquake rupture in oceanic lithosphere (Jackson et al., 2008). In the case of our numerical model, the important point is that as upwelling footwall material crosses the BDT, the flow field is already dominated by a solid-block rotational component (Fig.

2). Hence, there is no process of curvature increase (at least within the brittle-elastic regime) to produce the stress state envisaged in an elastic plate model. How deformation is resolved beneath the BDT (in order for this rotational flow to develop) is of little consequence, as the deviatoric stresses produced are negligible. In other words: rotation develops before strength. It is for this reason that the ODF curvature is representative of a neutral stress configuration, rather than a 'bent' one.

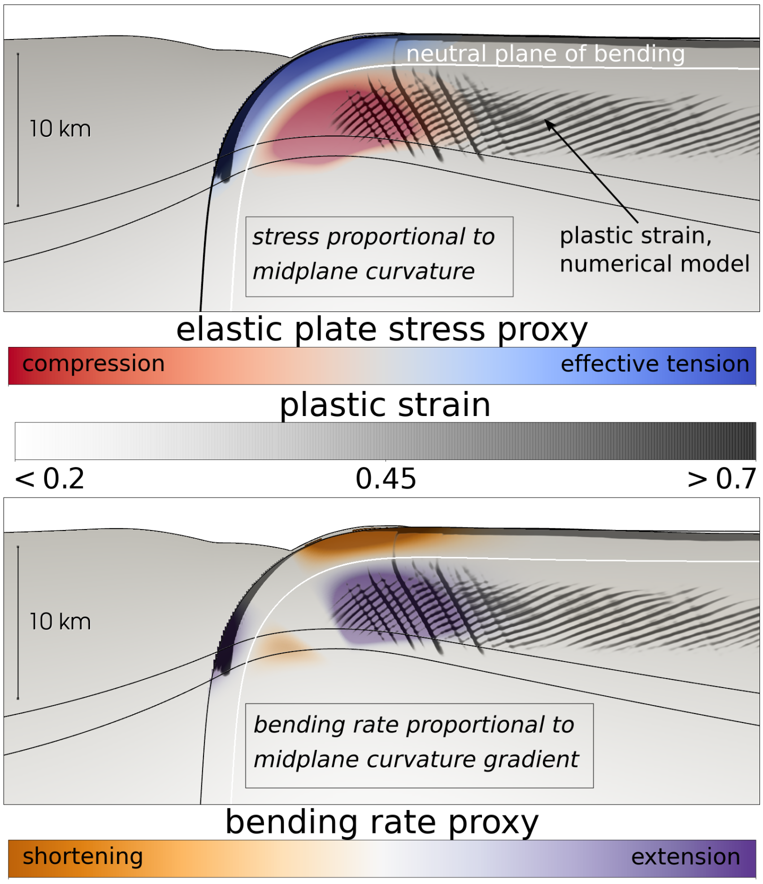

Figure 5. Contrast between a elastic plate relationship for footwall stress, based on the (static) curvature the ODF/OCC (top panel) and a kinematic view of exhumation, where apparent unbending is the dominant flexural process (bottom panel). A simple parameterisation of the detachment geometry (black line) provides the curvature (for the elastic plate relationship) and curvature gradient (for the advective bending rate relationship). In both panels, the white line represents the neutral plane of bending, positioned 2 km beneath the detachment surface, based on the location in our numerical model. All dynamic features (e.g. compression/shortening) are expressed relative to the neutral plane geometry. To generate the figure, the stress/bending rate magnitude was increased in proportion to the distance from the neutral plane, until reaching one of: a distance of 4 km, the detachment surface, or the 700 °C isotherm. At these points, the magnitude was rapidly tapered to zero. These are simply schematic representations designed to illustrate the differences between an elastic-plate view of stress (top panel, as discussed by Parnell-Turner et al. (2017), versus the flexural process that dominates our model (i.e. apparent unbending, bottom panel). In both figures the accumulated plastic strain from our reference numerical model is shown (at an elapsed time of 2.0 Myr) in transparent greyscale.

Moreover, once footwall material is exhumed beyond the zone of solid-block rotation, flexure occurs, following the trend of decreasing curvature in the OCC outboard of the detachment termination (i.e. apparent unbending). Counter-intuitively, material in the footwall of our numerical model undergoes virtually monotonic flexural strain with exactly the opposite polarity to that implied by the detachment curvature. These contrasts between an elastic plate model and the flexural bending rates that are associated with apparent unbending are highlighted in Fig. 5.

An important aspect of apparent unbending is that flexural deformation is present even when the morphology of the system is quasi-static. These strains arise because the advective rate of curvature, which is proportional to curvature gradients (e.g. Fig. 5), is non-zero (Kawakatsu, 1986; Sandiford et al., 2020). Apparent unbending is a kinematic, rather than a flexural-isostatic process. Unlike the strain rates, the stress state in the footwall (and hanging wall) will also remain influenced by the flexural-isostatic compensation of the axial valley in a steady-state configuration.

While the alternative numerical model (Fig. 4) shows a more complex evolution, exhumation is likewise dominated by solid-block rotation. Hence, the same general conclusions follow in regard to the fact that detachment curvature is a misleading proxy for flexural stress.

To our knowledge, the process of apparent unbending has not been discussed in previous modelling studies nor its relationship to solid-block rotation in detachment footwalls. Yet a number of previous numerical models show strain rate patterns consistent with this kinematic feature. Figures 2b&c of the 2d models of Tucholke et al. (2008) show a zone of high strain rate outboard of the surface ODF exposure. The geometry of this zone shows a characteristic triangular hourglass pattern, suggestive of flexural strain. A similar feature can be discerned in the 3d models of Howell et al. (2019), although the vertical exaggeration makes the pattern less clear. In both cases, only the magnitude of the stain rate tensor is shown (rather than its horizontal components), so the flexural nature of the deformation cannot be identified with complete confidence. Nevertheless, it appears that the kinematic processes we have identified in our model are evident in previous numerical modelling studies.

4.2 Flexure and brittle deformation in models

The accumulated plastic (pseudo-brittle) strain in the reference model is shown in Fig. 3 (at 1.5 Myr) and Fig. 5 (at 2.0 Myr). Comparing the zone of plastic strain accumulation with the sign of stress or strain rate horizontal components (e.g. Fig. 3) reveals that the plastic strain accumulated during exhumation is almost entirely generated by extensional-type structures in the region of apparent unbending. These patterns in the accumulated plastic strain show that while there is a flexural origin for most of the brittle strain in the detachment footwall, its seismic expression is expected to be dominated by normal faulting.

Earlier in the reference model development, footwall faulting is characterised by normal faults synthetic to the ODF (e.g Fig. 3 at 1.5 Myr). Later in the model, we see a systematic spatial trend where extension occurs on closely-spaced ODF-synthetic normal faults nearer the axial valley, moving outboard to more widely spaced antithetic faults. Note how in Fig. 5, these larger antithetic faults can be seen to offset the fabric developed by the synthetic-dipping faults. Ultimately, one of the major antithetic normal faults becomes the structure on which a new detachment fault forms, reversing the dip of the detachment (as is shown in Supplementary movie S1).

4.3 Observational constraints and predictions

In the previous sections we summarised kinematic and deformation patterns in our numerical models. We now discuss these patterns in connection to observations of seismicity from ODF/OCC segments. Recording small magnitude events and obtaining precise earthquake hypocenters in ODF regions generally requires hydrophone or ocean-bottom seismograph deployment. Hence, at this stage only a small number of pertinent studies exist (Demartin et al., 2007; Parnell-Turner et al., 2017; Collins et al., 2012; Grevemeyer et al., 2013; Parnell-Turner et al., 2020). Even fewer show a pattern of hypocenters in which a dominant asymmetric detachment is convincingly delineated, which would suggest a tectonic configuration analogous to our model setup.

Supplementary Fig. S1 shows map and cross-sectional views of the hypocenters at the TAG detachment from Demartin et al. (2007). In Fig. 3, we plot a narrow swathe (those epicenters ≤ 4.5 km of the line shown in Fig. S1) of the TAG earthquakes overlaid on the horizontal strain rate component from our model. This exercise suggests that important features of the TAG detachment seismicity can be explained by the kinematic and flexural patterns we have discussed. In particular, the combination of solid-block rotation beneath the detachment and apparent unbending beneath the OCC may explain why the TAG footwall directly beneath the ODF has sparse seismicity, while extensional seismicity is concentrated outboard of the termination. It can also explain why footwall seismicity is concentrated at depths greater than ~ 2 km beneath the sea floor (see Fig. S1 for location of seismicity relative to the TAG bathymetry).

Nevertheless, it is clear the footwall earthquake cluster imaged by Demartin et al. (2007) is significantly more limited in its spatial extent than compared to the region of high strain rates developed in the model (e.g. Fig 3). A few points are worth bearing in mind, however: the seismic deployment detailed in Demartin et al. (2007) was relatively short (eight months), and seismicity patterns may be biased with respect to the long-term tectonic strain rates; there may be additional variability in terms of whether faulting occurs as unstable sliding (e.g. earthquakes) versus stable slip (e.g. Mark et al. (2018)), as well as the level of micro-seismicity versus larger events (i.e. the b-value). Similarly, procedures on the numerical modelling side could be implicated: we omit physical processes such as melting, hydrothermal heat transport as well as any 3-dimensional aspects of dynamics which may effect thermal and dynamic structure of the footwall. Moreover, the constitutive models utilised in our simulations, convergence of associated nonlinearity, and the implications of mesh sensitivity, are areas of active research, debate and experimentation for the geodynamic discipline (e.g. Duretz et al. (2020)). It will therefore be important to explore whether the kinematic features we identify are equally prominent in the models of other groups that use different numerical approaches, constitutive models and physical approximations.

Our numerical models do not offer a ready explanation for compressional seismicity directly beneath the ODF, as reported by Parnell-Turner et al. (2017). However, these compressional earthquakes also exhibit significant variability in the orientation of the focal mechanism P-axes (unlike the cluster attributed to the detachment fault itself - Fig. 2C of that study). This is a potential indication that these earthquakes do not have a tectonic origin, or at least that the causes for deformation cannot be reduced to 2d plane-strain processes like elastic plate bending or apparent unbending. We note that in a follow-up study of this region, which also encompasses areas directly to the north, the vivid cluster of compressional events is completely absent (Parnell-Turner et al., 2020). Rather, this later study mainly captures earthquakes inferred to belong to the detachment faults, as well as streaks of activity outboard of the axial valley beneath the OCC/footwall. In the 13°30′N detachment region, for instance, clustering is broadly comparable to the TAG patterns, although event numbers are much smaller.

A prediction of our reference numerical model is that a small amount of shortening may occur in the shallowest few kilometers of OCCs, associated with the process of apparent unbending. The steep thrust structures that accommodate this strain have a total downdip extent of only a few kilometers, and they are expected to contribute a very minor part of the total seismic moment associated with footwall exhumation (see the patterns of accumulated plastic strain in Fig. 5). While such deformation may be difficult to capture in the short term seismic record, these steeply-dipping reverse faults represent the active structures that should intersect exposed OCCs, in places where they tend to flatten (curvature reduction) outboard of the detachment termination.

OCCs are known to be dissected by spreading-perpendicular faults, although there is clearly much variability, such as observed at the adjacent Mid Atlantic Ridge detachments at $\sim 13°20'$ N (no obvious dissecting faults) and $13°30'$ N (with dissecting faults), e.g. Parnell-Turner et al. (2018). These structures are usually inferred to be normal faults attributed to bending stresses during footwall rollover (Tucholke et al., 1998; Escartín et al., 2003), i.e. invoking an elastic plate stress relationship.

The alternative numerical model shows that footwall rotation during exhumation is not always associated with apparent unbending (i.e. Fig. 4 snapshot at 1.3 Myr). The transition from rotation to rigid plate translation can instead occur via a major through-going fault at the outboard edge of the block. Hence, our model results should not be interpreted as suggesting that all OCC footwalls must undergo apparent unbending and hence exhibit evidence of minor thrust faults. Rather, the key prediction of the models is that exhumation beneath concave-down ODFs is dominated by solid-block rotation. The zone of solid-block rotation must transition, via some pattern of deformation, to the outboard region of rigid plate translation. Our models show two modes in which this may occur. We suggest that where exposed OCCs reduce their curvature outboard of the ODF termination, yet remain largely coherent, the flexure should be associated with shortening, compressional stress accumulation, and minor thrust faults.

5 Conclusions

This study addresses the nature of footwall exhumation in ODF settings, based on results of high-resolution numerical models. Exhumation is characterised by a strong component of solid-block rotation, accommodated by the concave-down ODF. This has important implications for how flexural processes operate in the system. We demonstrate a relationship between flexural stress and detachment curvature that is very different to the elastic plate model previously typically assumed. Our model also helps differentiate between the static flexural stress component associated with regional compensation of the axial depression, and a kinematic component of flexure associated with the transition from solid-block rotation of the footwall to rigid plate translation (apparent unbending).

Our results suggest that flexure related to apparent unbending may provide a significant component of the extensional seismic moment in detachment footwalls. Whereas Parnell-Turner et al. (2017) argued that bending may cause 'compression in extension', our models rather suggests that bending may promote 'extension in extension'. The deformation patterns predicted in our model are broadly applicable to micro-seismicity patterns from the TAG detachment.

The geometry of detachment faults has classically been analysed from the perspective of fault mechanics and evolution, in which fault rotation and footwall rollover are associated with the flexural-isostatic response of the lithosphere to extension. Our model suggests that, while these processes are certainly important in the development of the detachment system, the system can evolve into a configuration that goes somewhat beyond the dynamics described in the flexural rotation model. In this configuration, the ODF geometry has a very specific relationship to the kinematics of exhumation, namely the accommodation of solid-block rotation of the footwall. The ODF in our models appears to be acting less as a classical fault and more in the sense of an exhumation channel (Brune et al., 2014). We speculate that minimization of distributed plastic strain may play a role in the ultimate geometric configuration of the ODF and the mechanics of exhumation; this provides one avenue for future research into these enigmatic plate boundary zones.

Acknowledgments

Figures were created using Pyvista, a Python interface for the Visualization Toolkit (VTK) (Sullivan & Kaszynski, 2019). DS, SB, and JMW were supported by Australian Research Council grant DP180102280. AG was supported by the Helmholtz Young Investigators Group CRYSTALS (grant no. VH-NG-1132). Data is available is available through Demartin et al. (2007) (10.1594/IEDA/306798).

References

Axen, G. J., & Hartley, J. M. (1997). Field tests of rolling hinges: Existence, mechanical types, and implications for extensional tectonics. *Journal of Geophysical Research: Solid Earth*, *102*(B9), 20515–20537.

Bangerth, W., Dannberg, J., Gassmoeller, R., & Heister, T. (2020, June). *Aspect v2.2.0.* Zenodo. Retrieved from `https://doi.org/10.5281/zenodo.3924604` doi: 10.5281/zenodo.3924604

Bangerth, W., Dannberg, J., Gassmöller, R., Heister, T., et al. (2020b, June). ASPECT: Advanced Solver for Problems in Earth's ConvecTion, User Manual. Retrieved from `https://doi.org/10.6084/m9.figshare.4865333` (doi:10.6084/m9.figshare.4865333) doi: 10.6084/m9.figshare.4865333

Brune, S., Heine, C., Pérez-Gussinyé, M., & Sobolev, S. V. (2014). Rift migration explains continental margin asymmetry and crustal hyper-extension. *Nature communications*, *5*(1), 1–9.

Buck, W. R. (1988). Flexural rotation of normal faults. *Tectonics*, *7*(5), 959–973.

Cannat, M. (1993). Emplacement of mantle rocks in the seafloor at mid-ocean ridges. *Journal of Geophysical Research: Solid Earth*, *98*(B3), 4163–4172.

Cannat, M., Sauter, D., Lavier, L., Bickert, M., Momoh, E., & Leroy, S. (2019). On spreading modes and magma supply at slow and ultraslow mid-ocean ridges. *Earth and Planetary Science Letters*, *519*, 223–233.

Chapple, W. M., & Forsyth, D. W. (1979). Earthquakes and bending of plates at trenches. *Journal of Geophysical Research: Solid Earth*, *84*(B12), 6729–6749.

Choi, E., Buck, W. R., Lavier, L. L., & Petersen, K. D. (2013). Using core complex geometry to constrain fault strength. *Geophysical Research Letters*, *40*(15), 3863–3867.

Collins, J. A., Smith, D. K., & McGuire, J. J. (2012). Seismicity of the atlantis massif detachment fault, 30° n at the mid-atlantic ridge. *Geochemistry, Geophysics, Geosystems*, *13*(10).

Demartin, B. J., Sohn, R. A., Canales, J. P., & Humphris, S. E. (2007). Kinematics and geometry of active detachment faulting beneath the trans-atlantic geotraverse (tag) hydrothermal field on the mid-atlantic ridge. *Geology*, *35*(8), 711–714.

Duretz, T., de Borst, R., Yamato, P., & Le Pourhiet, L. (2020). Toward robust and predictive geodynamic modeling: The way forward in frictional plasticity. *Geophysical Research Letters*, *47*(5), e2019GL086027.

Escartín, J., Mével, C., MacLeod, C. J., & McCaig, A. (2003). Constraints on deformation conditions and the origin of oceanic detachments: The mid-atlantic ridge core complex at 15 45 n. *Geochemistry, Geophysics, Geosystems*, *4*(8).

Escartín, J., Mevel, C., Petersen, S., Bonnemains, D., Cannat, M., Andreani, M., ... others (2017). Tectonic structure, evolution, and the nature of oceanic core complexes and their detachment fault zones (13 20 n and 13 30 n, mid atlantic ridge). *Geochemistry, Geophysics, Geosystems*, *18*(4), 1451–1482.

Garcés, M., & Gee, J. S. (2007). Paleomagnetic evidence of large footwall rotations associated with low-angle faults at the mid-atlantic ridge. *Geology*, *35*(3), 279–282.

Glerum, A., Thieulot, C., Fraters, M., Blom, C., & Spakman, W. (2018). Nonlinear viscoplasticity in aspect: benchmarking and applications to subduction. *Solid Earth*, *9*, 267–294.

Grevemeyer, I., Reston, T. J., & Moeller, S. (2013). Microseismicity of the mid-atlantic ridge at 7° s–8° 15 s and at the logatchev massif oceanic core complex at 14° 40 n–14° 50 n. *Geochemistry, Geophysics, Geosystems*, *14*(9), 3532–3554.

Heister, T., Dannberg, J., Gassmöller, R., & Bangerth, W. (2017). High accuracy mantle convection simulation through modern numerical methods. II: Realistic models and problems. *Geophysical Journal International*, *210*(2), 833-851. Retrieved from `https://doi.org/10.1093/gji/ggx195` doi: 10.1093/gji/ggx195

Howell, S. M., Olive, J.-A., Ito, G., Behn, M. D., Escartin, J., & Kaus, B. (2019). Seafloor expression of oceanic detachment faulting reflects gradients in mid-ocean ridge magma supply. *Earth and Planetary Science Letters*, *516*, 176–189.

Jackson, J., McKenzie, D., Priestley, K., & Emmerson, B. (2008). New views on the structure and rheology of the lithosphere. *Journal of the Geological Society*, *165*(2), 453–465.

Kawakatsu, H. (1986). Double seismic zones: kinematics. *Journal of Geophysical Research: Solid Earth*, *91*(B5), 4811–4825.

Kronbichler, M., Heister, T., & Bangerth, W. (2012). High accuracy mantle convection simulation through modern numerical methods. *Geophysical Journal International*, *191*, 12-29. Retrieved from `http://dx.doi.org/10.1111/j.1365-246X.2012.05609.x` doi: 10.1111/j.1365-246X.2012.05609.x

Lavier, L. L., Buck, W. R., & Poliakov, A. N. (2000). Factors controlling normal fault offset in an ideal brittle layer. *Journal of Geophysical Research: Solid Earth*, *105*(B10), 23431–23442.

MacLeod, C. J., Carlut, J., Escartín, J., Horen, H., & Morris, A. (2011). Quantitative constraint on footwall rotations at the 15° 45 n oceanic core complex, mid-atlantic ridge: Implications for oceanic detachment fault processes. *Geochemistry, Geophysics, Geosystems*, *12*(5).

MacLeod, C. J., Escartin, J., Banerji, D., Banks, G., Gleeson, M., Irving, D. H. B., … others (2002). Direct geological evidence for oceanic detachment faulting: The mid-atlantic ridge, 15 45 n. *Geology*, *30*(10), 879–882.

MacLeod, C. J., Searle, R., Murton, B., Casey, J., Mallows, C., Unsworth, S., … Harris, M. (2009). Life cycle of oceanic core complexes. *Earth and Planetary Science Letters*, *287*(3-4), 333–344.

Mark, H. F., Behn, M. D., Olive, J.-A., & Liu, Y. (2018). Controls on mid-ocean ridge normal fault seismicity across spreading rates from rate-and-state friction models. *Journal of Geophysical Research: Solid Earth*, *123*(8), 6719–6733.

Moresi, L., Dufour, F., & Mühlhaus, H.-B. (2003). A lagrangian integration point finite element method for large deformation modeling of viscoelastic geomaterials. *Journal of computational physics*, *184*(2), 476–497.

Morris, A., Gee, J., Pressling, N., John, B., MacLeod, C. J., Grimes, C., & Searle, R. (2009). Footwall rotation in an oceanic core complex quantified using reoriented integrated ocean drilling program core samples. *Earth and Planetary*

Science Letters, *287*(1-2), 217–228.

Müller, R. D., Seton, M., Zahirovic, S., Williams, S. E., Matthews, K. J., Wright, N. M., ... others (2016). Ocean basin evolution and global-scale plate reorganization events since pangea breakup. *Annual Review of Earth and Planetary Sciences*, *44*, 107–138.

Naliboff, J., Glerum, A., Brune, S., Péron-Pinvidic, G., & Wrona, T. (2020). Development of 3-d rift heterogeneity through fault network evolution. *Geophysical Research Letters*, *47*(13), e2019GL086611.

Olive, J.-A., Behn, M. D., Mittelstaedt, E., Ito, G., & Klein, B. Z. (2016). The role of elasticity in simulating long-term tectonic extension. *Geophysical Journal International*, *205*(2), 728–743.

Parnell-Turner, R., Escartin, J., Olive, J.-A., Smith, D. K., & Petersen, S. (2018). Genesis of corrugated fault surfaces by strain localization recorded at oceanic detachments. *Earth and Planetary Science Letters*, *498*, 116–128.

Parnell-Turner, R., Sohn, R., Peirce, C., Reston, T., MacLeod, C., Searle, R., & Simão, N. (2020). Seismicity trends and detachment fault structure at 13° n, mid-atlantic ridge. *Geology*.

Parnell-Turner, R., Sohn, R., Peirce, C., Reston, T., MacLeod, C. J., Searle, R., & Simão, N. (2017). Oceanic detachment faults generate compression in extension. *Geology*, *45*(10), 923–926.

Reston, T., & Ranero, C. R. (2011). The 3-d geometry of detachment faulting at mid-ocean ridges. *Geochemistry, Geophysics, Geosystems*, *12*(7).

Rose, I., Buffett, B., & Heister, T. (2017). Stability and accuracy of free surface time integration in viscous flows. *Physics of the Earth and Planetary Interiors*, *262*, 90 - 100. Retrieved from `http://dx.doi.org/10.1016/j.pepi.2016.11.007` doi: 10.1016/j.pepi.2016.11.007

Sandiford, D., Moresi, L. M., Sandiford, M., Farrington, R., & Yang, T. (2020). The fingerprints of flexure in slab seismicity. *Tectonics*, *39*(8), e2019TC005894.

Spencer, J. E. (1984). Role of tectonic denudation in warping and uplift of low-angle normal faults. *Geology*, *12*(2), 95–98.

Sullivan, C. B., & Kaszynski, A. (2019, may). PyVista: 3d plotting and mesh analysis through a streamlined interface for the visualization toolkit (VTK). *Journal of Open Source Software*, *4*(37), 1450. Retrieved from `https://doi.org/`

10.21105/joss.01450 doi: 10.21105/joss.01450

Tucholke, B. E. (1998). Discovery of" megamullions" reveals gateways into the ocean crust and upper mantle. *OCEANUS-WOODS HOLE MASS.-*, *41*, 15–19.

Tucholke, B. E., Behn, M. D., Buck, W. R., & Lin, J. (2008). Role of melt supply in oceanic detachment faulting and formation of megamullions. *Geology*, *36*(6), 455–458.

Tucholke, B. E., Lin, J., & Kleinrock, M. C. (1998). Megamullions and mullion structure defining oceanic metamorphic core complexes on the mid-atlantic ridge. *Journal of Geophysical Research: Solid Earth*, *103*(B5), 9857–9866.

Wernicke, B., & Axen, G. J. (1988). On the role of isostasy in the evolution of normal fault systems. *Geology*, *16*(9), 848–851.

Supporting Information for "Kinematics of footwall exhumation at oceanic detachment faults: solid-block rotation and apparent unbending"

Dan Sandiford[1,2], Sascha Brune[2,3], Anne Glerum[2], John Naliboff[4], Joanne M. Whittaker[1]

[1]Institute for Marine and Antarctic Studies, University of Tasmania, Hobart, Tasmania, Australia, 7004

[2]Helmholtz Centre Potsdam - German Research Centre for Geosciences (GFZ)

[3]Institute of Geosciences, University of Potsdam, Potsdam, Germany

[4]Department of Earth and Environmental Science, New Mexico Institute of Mining and Technology

Contents of this file

1. Text S1 to S2
2. Figure S1
3. Table S1

Additional Supporting Information (Files uploaded separately)

1. Captions for Movies S1 and S2
2. ASPECT parameter (.prm) file

Text S1: TAG seismicity

Fig. S1 shows map and cross-section views of the hypocenters from the Trans-Atlantic Geotraverse (TAG) detachment at the Mid-Atlantic Ridge, produced by Demartin et al. (2007). That study identified two distinct zones of seismic activity, one interpreted to represent the curved trace of the active detachment fault, and a second locus about 8 km outboard of the detachment cluster, suggested to relate to antithetic normal fault planes in the footwall. It is notable that microseismicity along the detachment is concentrated some 2-7 km beneath the seafloor. Craig and Parnell-Turner (2017) argue that the shallowest part of the TAG detachment (also the least-optimally oriented) tends to produce larger-magnitude earthquakes, and less microseismicity.

In map view, the TAG epicenters form a donut shape, with a prominent seismic gap in the footwall adjacent to the detachment fault termination at the seafloor. Focal mechanisms shown in Fig. S1 are representative, constructed from the dip values referred to in Demartin et al. (2007). Readers are referred to the original study for further details. In the manuscript (Fig. 3) the earthquakes plotted are those within a distance $\pm$ 4.5 km from the line A-A', which attempts to minimise the 3-D aspects of the full seismicity pattern.

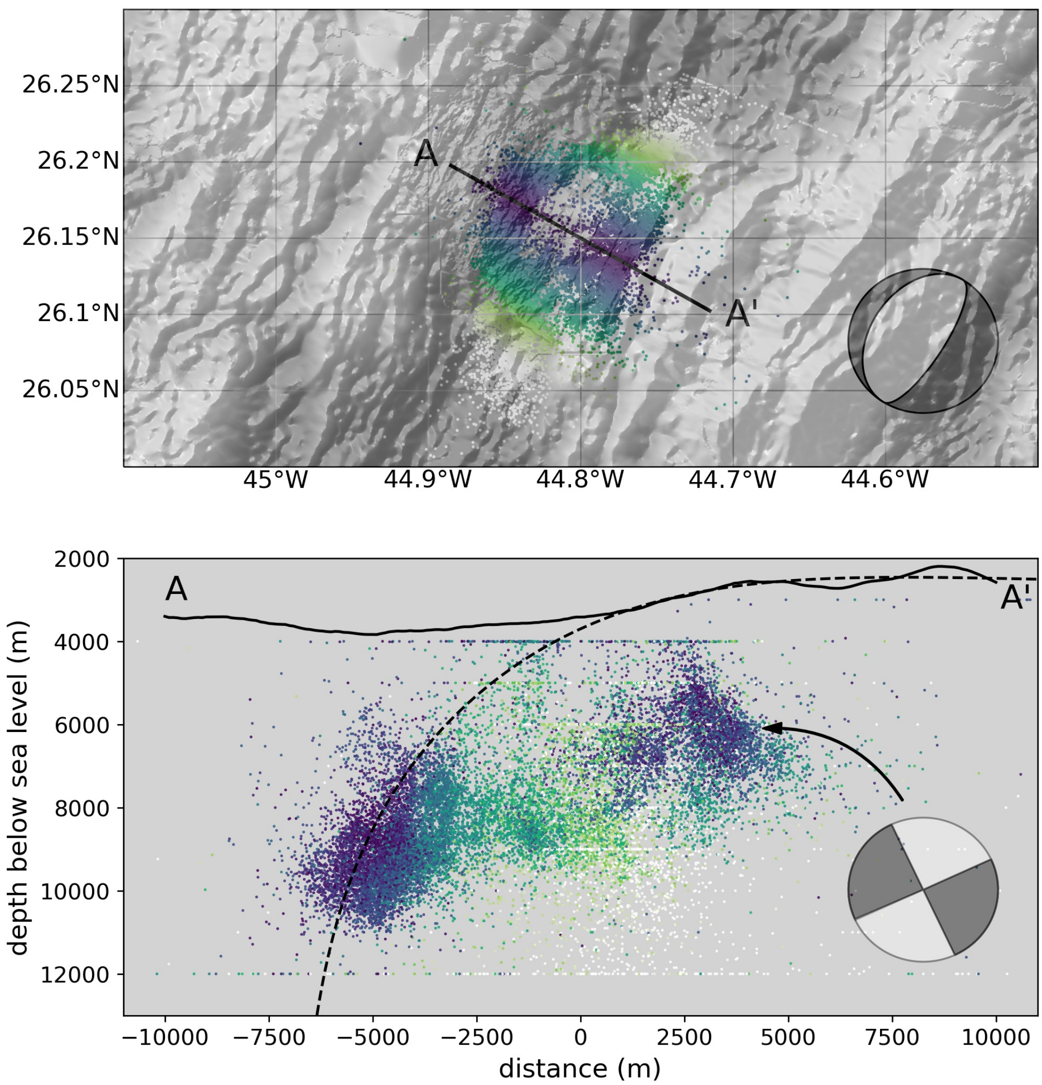

Figure S1. Hypocenters from the TAG detachment segment of the the Mid-Atlantic Ridge, from the study of Demartin et al. (2007). The distance of line between A-A' in the top panel is 20 km. Hypocenters are coloured to show relative distance from the line. Bottom panel shows a cross sectional view of the seismicity. The dashed line is a parameterization of the emergent detachment morphology from our numerical model.

Text S2: Numerical model methods

Thermo-mechanical model

We model the 2-D thermo-mechanical evolution of an amagmatic oceanic spreading center, using ASPECT to solve the incompressible Stokes and advection-diffusion equations, according to the Boussinesq approximations described in Bangerth et al. (2020b). Adiabatic and shear heating are thus neglected in the energy equation. Elastic shear deformation is included in the constitutive model, necessitating an additional force term in the Stokes equations (e.g. Schmalholz et al. (2001); Moresi et al. (2003); Bangerth et al. (2020)). There is no compositional differentiation in the model (e.g. crust versus mantle) and the constitutive model applies to all parts of the domain. The temperature dependence of the dislocation creep means that creep increasingly dominates at temperatures $\geq 600°$C, while colder parts of lithosphere are effectively elasto-brittle. The constitutive model is described in the following section.

Viscous creep

The effective viscosity associated with high temperature dislocation creep is modelled with a wet olivine flow law (Hirth & Kohlstedt, 2003):

$$\eta = \frac{1}{2} A^{-\frac{1}{n}} |D|^{\frac{1-n}{n}} \exp\left(\frac{E + pV}{nRT}\right) \tag{1}$$

$|D|$ is the square root of the second invariant (or magnitude) of the deviatoric strain rate tensor: $|D| = (D_{ij} D_{ij}/2)^{1/2}$. R is the gas constant, T is temperature, p is pressure, A is the prefactor, n is the stress exponent, E is the activation energy and V is the activation volume. Values are provided in Table S1.

The prefactor A is weakened linearly with accumulated viscous strain, following the same functional form as the brittle strength weakening (e.g. Eqn. 11, see also Naliboff et al. (2020)). Relevant parameters are given in Table S1.

Visco-elasticity

This section describes the implementation of Maxwell visco-elasticity within a Stokes flow framework, where the stress history is tracked in an Eulerian reference frame (as in ASPECT 2.2.0). Compared with a Lagrangian tracking scheme, such as described by Moresi et al. (2003), the key difference is that advective terms must be accounted for in the stress rate tensor.

In the Maxwell viscoelastic model, strain rates are proportional to the sum of the stress and stress rate. D_{ij}, is given by

$$D_{ij} = D^v_{ij} + D^e_{ij} = \frac{\tau_{ij}}{2\eta} + \frac{1}{2\mu}\frac{D\tau_{ij}}{Dt}. \tag{2}$$

Where τ_{ij} is the deviatoric part of the Cauchy stress tensor. To simplify the description in this section, we use η to refer to viscosity associated with dislocation creep (i.e. $\eta = \eta(T, p, |D|)$).

The constitutive relationship for a Maxwell viscoelastic fluid (Eqn. 2) contains the stress rate tensor. The temporal derivative in the stress rate is a material derivative and, as we will track the stress rate in a Eulerian reference frame, advective terms must be accounted for.

A further requirement is that the stress rate tensor remains objective to rotation experienced by the material parcels (see Schmalholz et al. (2001); R. J. Farrington (2017) for details). This problem is typically handled by adopting an objective stress rate, in order to enforce the objectivity. Following (Moresi et al., 2003), we employ the Zaremba-Jaumann definition of stress rate:

$$\frac{D\tau_{ij}}{Dt} = \frac{\partial \tau_{ij}}{\partial t} + v_k\frac{\partial \tau_{ij}}{\partial x_k} - W_{ik}\tau_{kj} + \tau_{ik}W_{kj}$$

(3)

where W is the spin tensor.

Following Schmalholz et al. (2001); Moresi et al. (2003), ASPECT 2.2.0 discretizes the temporal part of $\frac{D\tau_{ij}}{Dt}$ using backwards finite difference:

$$\frac{\partial \tau^t_{ij}}{\partial t} \approx \frac{\tau^t_{ij} - \tau^{t-\Delta t}_{ij}}{\Delta t}$$

(4)

Solving for τ^t:

$$
\begin{aligned}
D^t_{ij} &= \frac{1}{2\eta}\tau^t_{ij} + \frac{1}{2\mu}\left(\frac{\tau^t_{ij}}{\Delta t} - \frac{\tau^{t-\Delta t}_{ij}}{\Delta t} + v_k\frac{\partial \tau^{t-\Delta t}_{ij}}{\partial x_k} - W_{ik}\tau^{t-\Delta t}_{kj} + \tau^{t-\Delta t}_{ik}W_{kj}\right) \\
\left(\frac{\mu\Delta t}{\mu\Delta t\eta} + \frac{\eta}{\mu\Delta t\eta}\right)\tau^t_{ij} &= 2D^t_{ij} + \frac{1}{\mu}\left(\frac{\tau^{t-\Delta t}_{ij}}{\Delta t} + v_k\frac{\partial \tau^{t-\Delta t}_{ij}}{\partial x_k} - W_{ik}\tau^{t-\Delta t}_{kj} + \tau^{t-\Delta t}_{ik}W_{kj}\right) \\
\tau^t_{ij} &= \left(\frac{\mu\Delta t\eta}{\mu\Delta t + \eta}\right)\left(2D^t_{ij} + \frac{1}{\mu}\left(\frac{\tau^{t-\Delta t}_{ij}}{\Delta t} + v_k\frac{\partial \tau^{t-\Delta t}_{ij}}{\partial x_k} - W_{ik}\tau^{t-\Delta t}_{kj} + \tau^{t-\Delta t}_{ik}W_{kj}\right)\right) \\
\tau^t_{ij} &= \eta_{\text{eff}}\left(2D^t_{ij} + \frac{1}{\mu}\left(\frac{\tau^{t-\Delta t}_{ij}}{\Delta t} + v_k\frac{\partial \tau^{t-\Delta t}_{ij}}{\partial x_k} - W_{ik}\tau^{t-\Delta t}_{kj} + \tau^{t-\Delta t}_{ik}W_{kj}\right)\right)
\end{aligned}
$$

For brevity, define $\tilde{\tau}_{ij}$ as the stress history tensor advected and rotated into the configuration of the current timestep:

$$
\tilde{\tau}_{ij} = \left(\tau^{t-\Delta t}_{ij} + v_k\frac{\partial \tau^{t-\Delta t}_{ij}}{\partial x_k} - W_{ik}\tau^{t-\Delta t}_{kj} + \tau^{t-\Delta t}_{ik}W_{kj}\right) \tag{5}
$$

so that

The stress at timestep t is given by:

$$
\tau^t = \eta_{\text{eff}}\left(2D^t_{ij} + \frac{1}{\mu\Delta t}\tilde{\tau}_{ij}\right) \tag{6}
$$

The Stokes Equation, representing conservation of momentum at infinite Prandtl number, can then be modified as follows:

$$
(2\eta_{\text{eff}}D_{ij})_{,j} - p_{,i} = f_i - \frac{\eta_{\text{eff}}}{\mu\Delta t}\tilde{\tau}_{ij,j} \tag{7}
$$

Advection and rotation terms in the stress rate

In ASPECT v2.2.0 (Bangerth et al., 2020), the stress history tensor is stored (component wise) as a set of non-diffusive scalar compositional fields. In the current implementation a two-stage approach is used to approximate the Zaremba-Jaumann stress rate. The advection terms for each component of stress rate are handled by the ASPECT's default compositional field capability. Version 2.2.0 of ASPECT uses a 2nd order implicit time integration for the advection equations (BDF-2).

Whenever the components of the stress history tensor are accessed (e.g. by various ASPECT material models) the relevant advection terms for each component will already have been calculated. The rotation terms in the Zaremba-Jaumann stress rate are then applied in the 'elasticity' submodule

(`aspect/source/material_model/rheology/elasticity.cc`):

$$\tilde{\tau}_{ij}^{t} = \frac{1}{\mu}\left(\frac{\check{\tau}_{ij}^{t}}{\Delta t} - W_{ik}\check{\tau}_{kj}^{t} + \check{\tau}_{ik}^{t}W_{kj}\right) \tag{8}$$

Where $\check{\tau}_{ij}^{t}$ refers to the stress history tensor after advective terms have been handled.

At the completion of the Stokes solve and the progression to the next time step, the components of the stress history tensor need to be updated. This process is also handled using ASPECT's compositional field capability. The update increment to the stress history components are applied as a 'reaction term', i.e. a source term in the advection equation.

Following R. Farrington et al. (2014), instead of simply taking the stress history at $t-1$, we store the stress history term $\check{\tau}$ as a running average ($\bar{\tau}_{ij}$) defined as:

$$\bar{\tau}_{ij} = (1-\Phi)\tilde{\tau}_{ij} + \Phi\tau ij \tag{9}$$

where $\Phi = \Delta t_c/\Delta t_e < 1$.

Visco-elasto-plastic model

Plastic deformation is incorporated into the visco-elastic constitutive model, following Moresi et al. (2003). Brittle behaviour is modelled through a Drucker-Prager yield limit (τ_y) on the magnitude of the deviatoric stress:

$$\tau_y = p\, sin(\phi) + Ccos(\phi) \tag{10}$$

where p is the pressure. The cohesion (C) and friction angle (ϕ) are weakened with accumulated plastic strain (γ^p) according to:

$$C(\beta) = \beta C_1 + (1-\beta)C_0 \tag{11}$$

Where

$$\beta = min(1, \gamma^p/\gamma_0^c) \tag{12}$$

The model is initialised with plastic strain on the quadrature points, randomly sampled from a uniform distribution between 0 and 0.25.

Again we use the notation $\tilde{\tau}$ (omitting component indexes here for brevity) for the stress history tensor (advected and rotated into the configuration of the current timestep). Define an effective strain rate as:

$$D_{\mathrm{eff}} = 2D + \frac{1}{\mu \Delta t_e}\tilde{\tau} \tag{13}$$

with the magnitude given by: $|D| = (D_{ij}D_{ij}/2)^{1/2}$. The plastic effective viscosity is then defined as:

$$\eta_{\mathrm{p}} = \frac{\tau_y}{|D_{\mathrm{eff}}|} \tag{14}$$

Substituting (14) into the definition of the stress (Eqn. 6) shows that this definition of the plastic viscosity satisfies the yield stress (i.e. it produces the intended viscosity rescaling at each iteration).

The final viscosity η_{vep} is defined depending on whether the magnitude of the deviatoric stress tensor exceeds τ_y^t:

$$\eta_{\mathrm{vep}} = \begin{cases} \eta_{\mathrm{p}}, & |\tau^t| \geq \tau_y \\ \eta_{\mathrm{eff}}, & \text{otherwise} \end{cases}$$

A successive substitution (Picard) approach is used to resolve the nonlinearity in the material model. The maximum number of iterations is limited to 40.

Model parameters

Parameter name	**Value**	**Symbol**	**Units**
Model domain depth	100	-	km
Model domain width	400	-	km
Potential temperature	1573	T_p	K
Surface temperature	293	T_s	K
Viscosity minimum	1×10^{18}	-	Pa s
Viscosity maximum	1×10^{24}	-	Pa s
Dislocation creep volume	22×10^{-6}	V	$\mathrm{m^3\,mol^{-1}}$
Dislocation creep energy	520	E	$\mathrm{kJ\,mol^{-1}}$
Dislocation creep exponent	3.5	n	-
Initial dislocation creep prefactor	3.77×10^{-14}	A_0	$\mathrm{Pa^{-n}\,s^{-1}}$
Weakened dislocation creep prefactor	1.385×10^{-14}	A_1	$\mathrm{Pa^{-n}\,s^{-1}}$
Prefactor weakening interval	2	γ_0^A	-
Initial friction angle	30	ϕ_0	$^\circ$
Initial cohesion	20	C_0	MPa
Weakened friction angle	3	ϕ_1	-
Weakened cohesion	10	C_1	MPa
Friction angle weakening interval	6	γ_0^ϕ	-
Cohesion weakening interval	6	γ_0^C	-
Elastic shear moduli	10	μ	GPa
Thermal diffusivity	3×10^{-6}	-	km
Heat capacity	1000	C_p	$\mathrm{J\,K^{-1}\,kg^{-1}}$
Full spreading rate	2	-	$\mathrm{cm\,yr^{-1}}$
Elastic timestep	10^4	Δt_e	yr
Numerical timestep (max)	2×10^3	Δt_c	yr
Reference density	3300	ρ_0	$\mathrm{kg\,m^{-3}}$
Thermal expansivity	3.5×10^{-5}	α	$\mathrm{K^{-1}}$

Table S1. Parameters used in the reference model. See also the included ASPECT input file (`input_reference_model.prm`). The alternative model differs only in that $\gamma_0^\phi = \gamma_0^C = 2$.

Movie S1 and S2 Captions

Movie S1 shows evolution of the reference model. The top panel shows the horizontal component (D_{xx}) of the strain rate tensor for the reference model, at times labelled. The model velocity field is shown with arrows. The bottom panel shows the vorticity, along with the accumulated plastic strain in greyscale, saturated at a value of 0.7. Bottom panel also shows vectors of the translated velocity field (velocity in the hanging wall reference frame). The two black lines in each panel show contours of the temperature field at 600 and 700 °C.

Movie S2 shows evolution of alternative model, where the strain intervals that determine plastic strength weakening are reduced. All features shown are identical to Movie S1.

References

Bangerth, W., Dannberg, J., Gassmoeller, R., & Heister, T. (2020, June). *Aspect v2.2.0.* Zenodo. Retrieved from `https://doi.org/10.5281/zenodo.3924604` doi: 10.5281/zenodo.3924604

Bangerth, W., Dannberg, J., Gassmöller, R., Heister, T., et al. (2020b, June). ASPECT: Advanced Solver for Problems in Earth's ConvecTion, User Manual. Retrieved from `https://doi.org/10.6084/m9.figshare.4865333` (doi:10.6084/m9.figshare.4865333) doi: 10.6084/m9.figshare.4865333

Craig, T. J., & Parnell-Turner, R. (2017). Depth-varying seismogenesis on an oceanic detachment fault at 13 20 n on the mid-atlantic ridge. *Earth and Planetary Science Letters*, *479*, 60–70.

Demartin, B. J., Sohn, R. A., Canales, J. P., & Humphris, S. E. (2007). Kinematics and geometry of active detachment faulting beneath the trans-atlantic geotraverse (tag) hydrothermal field on the mid-atlantic ridge. *Geology*, *35*(8), 711–714.

Farrington, R., Moresi, L.-N., & Capitanio, F. A. (2014). The role of viscoelasticity in subducting plates. *Geochemistry, Geophysics, Geosystems*, *15*(11), 4291–4304.

Farrington, R. J. (2017, 10). Geodynamic models of lithospheric and mantle processes. Retrieved from `https://bridges.monash.edu/articles/thesis/Geodynamic_models_of_lithospheric_and_mantle_processes_/4644928` doi: 10.4225/03/58a158e99e4df

Hirth, G., & Kohlstedt, D. (2003). Rheology of the upper mantle and the mantle wedge: A view from the experimentalists. *Geophysical Monograph-American Geophysical Union*, *138*, 83–106.

Moresi, L., Dufour, F., & Mühlhaus, H.-B. (2003). A lagrangian integration point finite element method for large deformation modeling of viscoelastic geomaterials. *Journal of computational physics*, *184*(2), 476–497.

Naliboff, J., Glerum, A., Brune, S., Péron-Pinvidic, G., & Wrona, T. (2020). Development of 3-d rift heterogeneity through fault network evolution. *Geophysical Research Letters*, *47*(13), e2019GL086611.

Schmalholz, S., Podladchikov, Y., & Schmid, D. (2001). A spectral/finite difference method for simulating large deformations of heterogeneous, viscoelastic materials. *Geophysical Journal International*, *145*(1), 199–208.